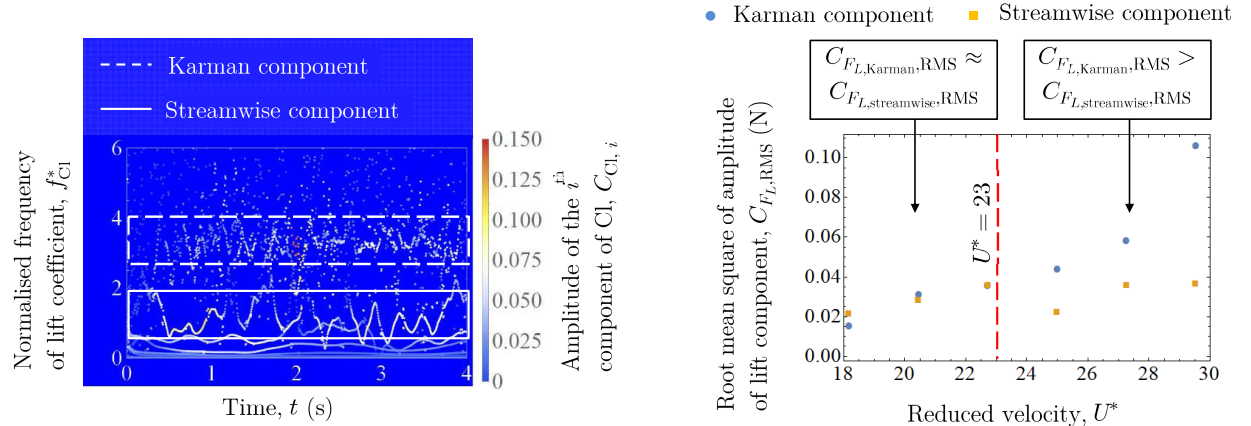


1 Graphical Abstract

2 Temporal Evolution of Lift in a Pure Cruciform System for Energy Harvesting

3 Ahmad Adzlan,Mohamed Sukri Mat Ali,Sheikh Ahmad Zaki



4 Highlights

5 Temporal Evolution of Lift in a Pure Cruciform System for Energy Harvesting

6 Ahmad Adzlan,Mohamed Sukri Mat Ali,Sheikh Ahmad Zaki

- 7 • We studied the vortex-induced vibration (VIV) of a cruciform system consisting of a circular cylinder and a
8 strip plate, and observed two distinct vibration regimes: the Karman vortex-induced vibration (KVIV) regime
9 between reduced velocities 2.3 and 13.6, and the streamwise vortex-induced vibration (SVIV) regime between
10 reduced velocities 15.9 and 29.5.
- 11 • Decomposition of the lift coefficient signal via ensemble empirical mode decomposition (EEMD) brings to the
12 fore the components of lift generated by the shedding of Karman and streamwise vortices, which in its origi-
13 nal form is observed as one non-monochromatic lift signal in the streamwise vortex-induced vibration (SVIV)
14 regime.
- 15 • Determination of phase lag between lift and cylinder displacement using Hilbert-Huang transform (HHT) showed
16 how the onset of streamwise vortex shedding brings about a higher level of intermittency into the cylinder dis-
17 placement and lift signals, in stark contrast to the highly regular and self-similar oscillation of the cylinder and
18 alternating lift acting upon it in the KVIV regime.
- 19 • Contribution to the total root-mean-square (RMS) lift amplitude from the shedding of both Karman and stream-
20 wise vortices suggest that we might be able to enlarge the RMS amplitude of lift – and as a result, harnessed
21 power – if we can redirect energy away from Karman vortices towards streamwise vortices, in the SVIV regime.

22 Temporal Evolution of Lift in a Pure Cruciform System for Energy 23 Harvesting

24 Ahmad Adzlan^{a,b,*}, Mohamed Sukri Mat Ali^a and Sheikh Ahmad Zaki^a

25 ^aMalaysia-Japan International Institute of Technology, Universiti Teknologi Malaysia, 54200 Kuala Lumpur, Malaysia

26 ^bFaculty of Engineering, Universiti Malaysia Sarawak, 94300 Kota Samarahan, Sarawak, Malaysia

27

28 ARTICLE INFO

31 **Keywords:**

32 Vortex-induced vibration

33 Vibration energy harvester

34 CFD simulation

35 Streamwise vorticity

36 Ensemble empirical mode decompo-

37 sition (EEMD)

38 Hilbert transform

39

40

41

42

43

44

ABSTRACT

We investigated the displacement and lift time series of a circular cylinder - strip plate cruciform system for energy harvesting in the Reynolds number range $1.1 \times 10^3 \leq Re \leq 14.6 \times 10^3$, numerically using the open source C++ library: OpenFOAM. The Karman vortex-induced vibration (KVIV) regime was identified between reduced velocity, U^* , 2.3 and 13.6, while the streamwise vortex-induced vibration (SVIV) regime was identified between $18.2 \leq U^* \leq 29.5$. We analysed the cylinder displacement and lift time series using the Hilbert-Huang transform (HHT). Within this range of U^* , Karman vortex shedding contributes nearly as much as streamwise vortex shedding to the root-mean-square amplitude of total lift, while between $25.0 \leq U^* \leq 29.5$, the Karman component contribution is on average twice that of the streamwise component. These findings hint at the possibility to improve the power output of the harvester by a factor of two between $18.2 \leq U^* \leq 22.7$ and by a factor of three between $25.0 \leq U^* \leq 29.5$, if we can unite the contribution to the root-mean-square amplitude of the total lift under a single vibration-driving mechanism: the shedding of streamwise vortex.

45 1. Introduction

46 Streamwise vortex-induced vibration (SVIV) is a type of vortex-induced vibration (VIV) driven by vortical struc-
47 tures whose vorticity vector points in the direction of the free stream. In recent decades, there have been efforts to
48 exploit the SVIV phenomenon from cruciform structures for energy harvesting, an example of which is given in Fig.
49 1. The literature on this subject can be broadly categorised into two groups: how the mechanical properties of the
50 oscillator (e.g., mass ratio, damping, etc.) affects the amplitude/frequency response of SVIV (Koide et al., 2009, 2013;
51 Nguyen et al., 2012) and how the minutiae of the flow field affect the force driving the vibration of the cylinder, i.e.
52 the fluid mechanical aspect of the system (Deng et al., 2007; Koide et al., 2017; Zhao and Lu, 2018).

53 In the first focus area, researchers studied some permutation of the following method to convert the vibration into
54 electrical power. The method consists of a coil and magnet. The coil, which moves with the vibrating cylinder, creates
55 relative motion against the magnet, which is placed in the hollow of the coil (Koide et al., 2009). While investigating
56 the system at a Reynolds number in the order of $Re \sim O(10^4)$, Koide et al. (2009) showed that increased damping
57 due to energy harvesting reduces the maximum vibration amplitude close to a factor of 4. Amplitude reduction due to
58 increased total damping was also mentioned in Bernitsas et al. (2008); Bernitsas and Raghavan (2008); Bernitsas et al.
59 (2009). Further investigation in Nguyen et al. (2012) revealed that damping not only affects the amplitude response of

*Corresponding author

 aafkhairi@graduate.utm.my (A. Adzlan); sukri.kl@utm.my (M.S.M. Ali); sheikh.kl@utm.my (S.A. Zaki)
ORCID(s): 0000-0003-0290-3185 (A. Adzlan); 0000-0001-6411-9965 (S.A. Zaki)

60 the cylinder but also narrows the synchronisation region between vortex shedding and cylinder vibration. Moreover,
 61 Nguyen et al. (2012) demonstrated a strong coupling between mass ratio and damping in determining both the width
 62 of the synchronisation region and the maximum amplitude response of the cylinder.

63 In the second focus area, investigators turned their attention to the details of the flow where streamwise vortex
 64 shedding occurs. One such study carefully shot motion pictures of the dye-injected flow (Koide et al., 2017) at Reynolds
 65 number in the order of $Re \sim O(10^3)$. A lower Reynolds number (Re) reduces the amount of turbulence in the flow,
 66 allowing a clearer shot of the vortex structures. Their study also highlights the higher level of turbulence produced
 67 by the circular cylinder-strip plate cruciform in contrast to the twin circular cylinder cruciform, which diminishes the
 68 periodicity of vortex shedding. Although visually enlightening, this and other more qualitative studies contribute little
 69 towards improving our understanding of the relationship between vortex shedding and the resulting lift. Deng et al.
 70 (2007) demonstrated a way to overcome such a shortcoming.

71 In their study, Deng et al. (2007) examined the flow field of a twin circular cylinder cruciform using computational
 72 fluid dynamics (CFD). Their domain stretches $28D$ in the streamwise direction, $16D$ in the transverse direction and
 73 $12D$ in the spanwise direction. They studied an Re range yet another order of magnitude smaller than that studied by
 74 Koide et al. (2017), possibly to get an even clearer visualisation of the vortical structures with less turbulence, and to
 75 ease computational requisites. At a fixed $Re = 150$, streamwise vortices form even at a gap ratio of 2. This result
 76 differs quite strikingly from Koide et al. (2006, 2007), conducted at an Re twice the order of magnitude of Deng et al.
 77 (2007), an indication that the minimum gap ratio needed for the onset of streamwise varies with respect to Re .

78 They also observed that when the gap ratio G , which they denote as L/D in their paper, increases from 3 to 4,
 79 the maximum amplitude of the lift coefficient increases by almost threefold. This can be attributed quite easily to the
 80 current vortex pair shed by the upstream cylinder. The downstream cylinder immediately disturbs the pair shed from
 81 the upstream cylinder when $G = 3$. The lift coefficient increases by about a factor of 3 when this immediate disturbance
 82 diminishes at $G = 4$. The visualisation of three-dimensional (3D) vorticity isocontours enables us to quickly establish
 83 this link vis-à-vis the lift coefficient signal. The authors use of CFD made this possible.

84 A similar study in the order of magnitude $Re \sim O(10^2)$ by Zhao and Lu (2018) particularly highlighted the
 85 immense utility of CFD as a tool to research SVIV or flow around a cruciform in general. They computed the sectional
 86 lift coefficient along the upstream cylinder, and the time history of this sectional lift coefficient revealed two different
 87 modes of vortex shedding, namely, parallel and K-shaped. They also paid attention to the local flow patterns that vary
 88 along the length of the upstream cylinder such as the trailing vortex flow, necklace vortex flow and flow in the small gap
 89 (denoted as SG flow). The discontinuities in the phase angle of the sectional lift coefficient along the upstream cylinder
 90 seems to suggest the inadequateness of attributing the lift coefficient to streamwise vortex shedding alone, particularly
 91 when Karman vortex streamlines were also observed some distance away from the junction of the cruciform. Shirakashi

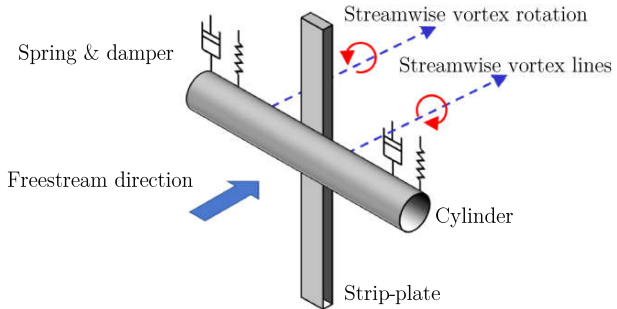


Figure 1: A schematic of the circular cylinder-strip plate cruciform system. Alternate shedding of the streamwise vortices create the alternating lift that drives the vibration of the cylinder.

et al. (1989) also made a similar observation in their experimental work. This leads us to hypothesise that the lift signal is more appropriately viewed as the streamwise-Karman vortex-induced composite lift signal. However, we could not find studies that took this viewpoint and worked out its implication on power generation in their investigation of SVIV.

The objectives of this study are thus threefold: (1) to take a closer look at the amplitude and frequency response of a circular cylinder-strip plate cruciform, especially in reduced velocity (U^*) ranges where the transition from KVIV to SVIV occurs, (2) to demonstrate the compositeness of the lift signal of an SVIV system and establish the difference between the lift signal characteristics in the KVIV and SVIV regime and (3) to shed light on how the contribution from the Karman and streamwise components of lift changes as we increase U^* after the onset of SVIV and predict how much improvement in the power generation can be anticipated if we are able to unify the lift amplitude contributions due to Karman and streamwise vortex shedding. Here, $U^* = U/f_n D$, with U , f_n and D being the freestream velocity, natural frequency of the system and the diameter of the circular cylinder respectively. The following §2 details the methodology we employ to conduct this study. We present and discuss our results in §4, §5, and §6. We describe our conclusions in §7.

2. Methodology

2.1. Problem geometry

The geometrical setup for this study builds on the work of Maruai et al. (2017, 2018) who studied both experimentally and numerically the FIM of a square cylinder with a downstream flat plate. Their simulation results are in good agreement with their own experiment, and with the experimental results of Kawabata et al. (2013), in the Reynolds number range $3.6 \times 10^3 < Re < 12.5 \times 10^3$. This is well within the Reynolds number studied in this work, i.e. $1.1 \times 10^3 < Re < 14.6 \times 10^3$.

Our $x - y$ plane fundamentally follows the dimensions used in Maruai et al. (2017, 2018), except for the cylinder shape, which in this study is circular, and the $20D$ distance to the outlet is measured from the downstream face of the

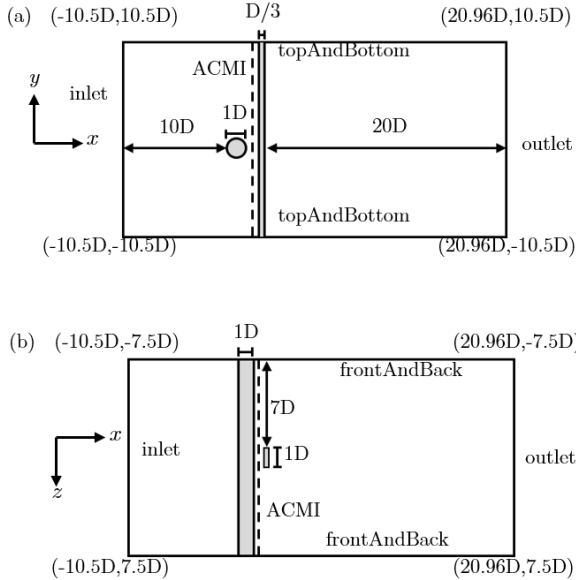


Figure 2: Problem geometry and coordinate system used. Figure 2a shows the side view of the simulation domain (cross-section perpendicular to the freestream) while Fig. 2b shows the top view of the simulation domain (cross-section parallel to the freestream). Note that the gap ratio G between the cylinder and the strip plate is $0.16D$, and the arbitrarily coupled mesh interface (ACMI) patch is located midway through the gap, i.e., $0.08D$ downstream from the trailing edge of the cylinder.

strip-plate. This is shown in Fig. 2. We chose the cylinder-plate gap G to be $0.16D$, as Koide et al. (2013) has shown that this gap size sustains the highest SVIV amplitude over the widest range of U^* , in comparison to other gap sizes.

As the problem geometry is explicitly three-dimensional (3D), the $x - y$ plane is extruded in the z direction, thus obtaining a 3D domain. As can be seen in Fig. 2, the circular cylinder extends from $z/D = 7.5$ to $z/D = -7.5$, while the strip-plate extends from -10.5 to $y/D = 10.5$. The z -direction extent is set as $z/D = \pm 7.5$ is already more than twice the spanwise reach of the streamwise vortex, thus sufficient for the vortices to materialise in our numerical solution. To compare, the spanwise extent of the numerical study by Deng et al. (2007), is $z/D = \pm 6$ and the spanwise extents of experiments by Nguyen et al. (2012) and Koide et al. (2013) are $z/D = \pm 5$.

2.2. Numerical method

The objectives of our study necessitate the solution of the continuity, and 3D unsteady Reynolds averaged Navier-Stokes (3D URANS) equations. We achieve this by using OpenFOAM, an open-source computational fluid dynamics (CFD) platform written in C++. Specifically, we work to solve the following continuity and URANS equations.

$$\frac{\partial U_i}{\partial x_i} = 0, \quad (1)$$

$$\frac{\partial U_i}{\partial t} + U_j \frac{\partial U_i}{\partial x_j} = -\frac{1}{p} \frac{P}{x_i} + \frac{\partial}{\partial x_j} \left(2\nu S_{ij} - \overline{u'_j u'_i} \right). \quad (2)$$

126 The symbols U , x , t , ρ , P , ν , S , and u' are the mean component of velocity, spatial component, time, density,
 127 pressure, kinematic viscosity, mean strain rate and the fluctuating component of velocity, respectively. The mean
 128 strain rate S_{ij} is given by

$$S_{ij} = \frac{1}{2} \left(\frac{\partial U_i}{\partial x_j} + \frac{\partial U_j}{\partial x_i} \right). \quad (3)$$

129 This study employs the Spalart-Allmaras turbulence model to approximate the Reynolds stress tensor $\tau_{ij} = \overline{u'_j u' i}$.
 130 This turbulence model has been shown to produce results that agree reasonably well with experiments in similar flow-
 131 induced motion (FIM) studies (Ding et al., 2015a,b). We use the Boussinesq approximation to relate the Reynolds
 132 stress tensor to the mean velocity gradient

$$\tau_{ij} = 2\nu_T S_{ij}, \quad (4)$$

133 where ν_T represents the kinetic eddy viscosity. ν_T is, in turn, a function of \tilde{v} and f_{v1} , while f_{v1} is a function of χ and
 134 c_{v1} , and χ a function of \tilde{v} and v , as shown in Eq. 5.

$$\nu_T = \tilde{v} f_{v1}, \quad (5a)$$

$$f_{v1} = \frac{\chi^3}{\chi^3 + c_{v1}^3}, \quad (5b)$$

$$\chi = \frac{\tilde{v}}{v}. \quad (5c)$$

135 Here, \tilde{v} serves to mediate the turbulence model and dictates how \tilde{v} is conserved.

$$\begin{aligned} \frac{\partial \tilde{v}}{\partial t} + U_j \frac{\partial \tilde{v}}{\partial x_j} &= c_{b1} \tilde{S} \tilde{v} - c_{w1} f_w \left(\frac{\tilde{v}}{D} \right)^2 \\ &+ \frac{1}{\sigma} \left\{ \frac{\partial}{\partial x_j} \left[(v + \tilde{v}) \frac{\partial \tilde{v}}{\partial x_j} \right] c_{b2} \frac{\partial \tilde{v}}{\partial x_i} \frac{\partial \tilde{v}}{\partial x_i} \right\} \end{aligned} \quad (6)$$

¹³⁶ c_{b1} , c_{b2} , and c_{v1} are constant with values 0.1335, 0.622 and 7.1 respectively. c_{w1} is given by

$$c_{w1} = \frac{c_{b1}}{\kappa} + \frac{1 + c_{b2}}{\sigma}, \quad (7)$$

¹³⁷ where additional constants κ and σ are 0.41 and 2/3 respectively. f_w , on the other hand, is given by

$$f_w = g \left(\frac{1 + c_{w3}^6}{g^6 + c_{w3}} \right)^{\frac{1}{6}}. \quad (8)$$

¹³⁸ Here, $c_{w3} = 2$ while g is given by

$$g = r + c_{w2} (r^6 - r), \quad (9)$$

¹³⁹ where r is

$$r = \min \left(\frac{\tilde{v}}{\tilde{S}\kappa^2 d^2}, 10 \right), \quad (10)$$

¹⁴⁰ Additionally, \tilde{S} is

$$\tilde{S} = \Omega + \frac{\tilde{v}}{\kappa^2 d^2} f_{v2}, \quad (11)$$

¹⁴¹ where Ω and d are the magnitude of vorticity and the distance from the mesh nodes to the nearest wall, respectively.

¹⁴² Finally, f_{v2} is

$$f_{v2} = 1 - \frac{\chi}{1 + \chi f_{v1}}. \quad (12)$$

¹⁴³ We solve these equations numerically using the PIMPLE algorithm, which combines the transient solver PISO with

¹⁴⁴ the steady-state solver SIMPLE for improved numerical stability.

145 2.3. Dynamic mesh motion

146 In this study, the cylinder in VIV moves perpendicular to the free stream direction. The motion unavoidably
147 distorts the mesh around it, degrading important mesh metrics such as non-orthogonality and skewness. However, we
148 can diffuse the mesh deformation to the neighbouring nodes as per the following Laplace equation,

$$\nabla \cdot (\gamma \nabla u) = 0. \quad (13)$$

149 Here, u represents the mesh deformation velocity and γ is displacement diffusion. We chose $\gamma = 1/l^2$, where l is the cell
150 centre distance to the nearest cylinder edges. We implement the GAMG linear solver with the Gauss-Seidel smoother to
151 solve Eq. 13. The dynamic mesh algorithm then updates the mesh node positions according to the following equation.

$$x_{\text{new}} = x_{\text{old}} + u\Delta t \quad (14)$$

152 The solver resumes the solution of Eqs. 1 and 2 once the mesh node positions are updated.

153 Another dynamic mesh handling technique used in this study is the arbitrarily coupled mesh interface (ACMI) that
154 allows non-conforming meshes to slide over another, thus preserving the mesh quality around a moving object. The
155 tiny gap between the cylinder and strip-plate, limits our ability to diffuse the mesh deformation to the surrounding
156 space. ACMI is thus implemented at the centre of the gap between the circular cylinder and the strip-plate, as shown in
157 Fig. 2, to circumvent this problem. This method has been successfully implemented in the works of Ding et al. (2015b);
158 Zhang et al. (2018), preserving the quality of their mesh and controlling their Courant-Friedrichs-Lowy (CFL) number.

159 2.4. Open flow channel experiment

160 We set up an experimental rig to validate our numerical results at reduced velocity $U^* = 22.7$. We chose $U^* = 22.7$
161 because that value of U^* is where the vibration-driving mechanism is known to transit from Karman to streamwise
162 vortex shedding (Koide et al., 2013). The experimental rig consists of a closed-loop open channel circuit based on the
163 water tunnel used by Nguyen et al. (2012), shown in Fig. 3. The cross-section of our test section is a square with sides
164 100 mm in length. The test section is 1500 mm long.

165 The system for providing elastic support and damping to the circular cylinder follows closely those used by Kawa-
166 bata et al. (2013) and Koide et al. (2013, 2017), which can be summarised as follows. The stiffness coefficient k of
167 the plate spring is determined through a simple weight versus displacement test (Sun et al., 2016), at various active
168 lengths of the spring. This provides a calibration curve of stiffness coefficient, k against plate spring length, l . We can

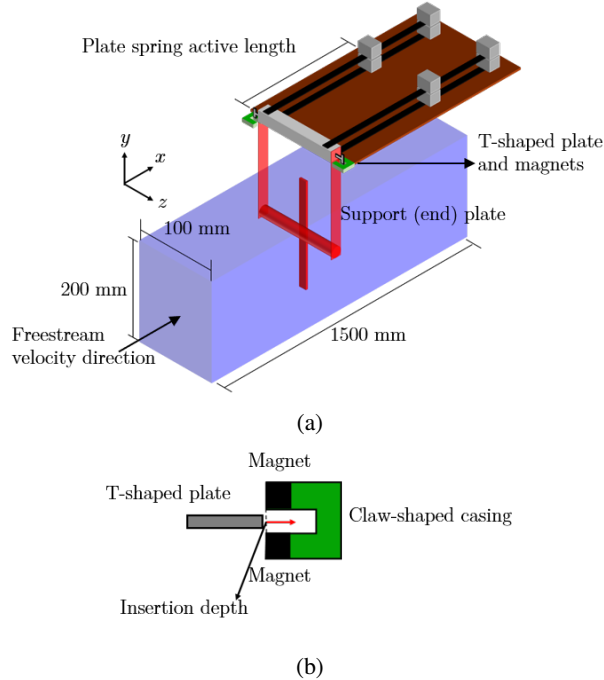


Figure 3: A schematic of our experimental setup. Figure 3a presents a 3D schematic of the experimental rig while Fig. 3b shows an enlarged schematic of the damping system.

169 then adjust the length of the plate spring to obtain the desired value for k .

170 On the other hand, the damping of the system is adjusted using T-shaped aluminium plates fixed at either end of
 171 the cylinder endplate, and a pair of neodymium magnets contained in a claw-shaped casing. The further the T-shaped
 172 plate is pushed into the opening of the claw, the denser the magnetic field it needs to cut through during motion, thus
 173 dissipating more energy. We then calibrate the damping produced at various depths at which the T-shaped plate is
 174 pushed into the casing, via free-decay tests of the cylinder in still water. The procedure for conducting free-decay tests
 175 are detailed in Raghavan (2007).

176 Flow inside the open channel is driven by a 3.728 kW (5 hp) centrifugal pump, controlled using a voltage controller.
 177 The input voltage for the centrifugal pump is calibrated against the centreline velocity of the test section, 750 mm from
 178 the inlet, i.e. mid-length of the test section. We show this schematically in Fig. 4. Here, we define the centreline of the
 179 test section as the line 50 mm from the bottom and 50 mm from either of the sidewalls of the test section. We placed the
 180 cylinder in the same position during experimental runs. The centreline velocity U_{cent} is measured using an acoustic
 181 Doppler velocimeter (ADV), sampling at 200 Hz. The resulting calibration curve is applicable for determining U_{cent} .
 182 at input voltages $30 < V_{\text{in}}(\text{V}) < 100$. We measured the turbulence intensity along the centreline to be about 5%.

183 We obtained the time history for cylinder displacement, y , by using a video camera pointed normal to the cylinder
 184 endplate. We placed a visual marker on the endplate, and the motion of the marker captured by the camera is analysed

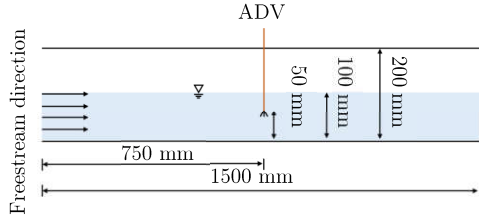


Figure 4: Side view of the open flow channel, in schematic form. Also, key dimensions of the experimental setup. The acoustic Doppler velocimeter (ADV) is placed at the same location where the cylinder is located during experimental runs.

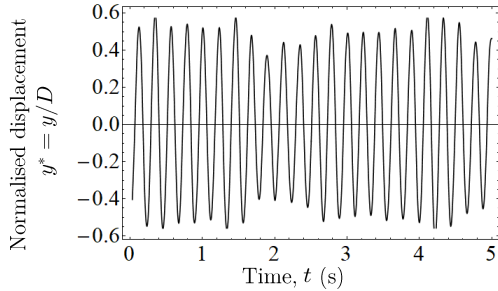


Figure 5: A sample of the time history for cylinder displacement from a test run of our experimental setup. The value of reduced velocity is $U^* = 22.7$.

185 using *Tracker*: a motion analysis tool built on the Open Source Physics Java framework. To validate our experimental
 186 setup, we tuned to the best of our ability our experimental parameters to the values used by Koide et al. (2013) and test
 187 whether we can replicate their results. Table 1 summarises the parameters in lieu of that paper.

Table 1

Summary of experimental parameters in contrast to those used in the experimental work of Koide et al. (2013).

	Current study	Koide et al. (2013)
Cylinder diameter, D (m)	0.01	0.01
Cylinder length, l_{cylinder} (m)	0.09	0.098
Strip-plate width (m)	0.01	0.01
Strip-plate length (m)	0.1	0.1
Effective mass, m_{eff} (kg)	0.162	0.174
Logarithmic damping, δ	0.178	0.24
Scruton number, Sc	9.94	7.74
System natural frequency, f_n (Hz)	4.42	4.4 to 4.79

188 We show a sample of the normalised displacement – $y^* = y/D$ – time series in Fig. 5. Computing the statistics of
 189 y^* and the normalised cylinder vibration frequency, $f^* = f_{\text{cyl}}/f_n$ (f_{cyl} being the vibration frequency of the cylinder),
 190 from several runs gave us a value of $y^* = 0.33 \pm 0.03$ and $f^* = 1.03 \pm 0.04$. Koide et al. (2013) obtained $y^* = 0.32$
 191 and $f^* = 1.09$ under a similar U^* condition. We thus take this fairly successful reproduction of the results of Koide
 192 et al. (2013) as an indication of readiness for further data collection.

¹⁹³ **3. Numerical setup validation**

¹⁹⁴ **3.1. Simple grid independency study**

¹⁹⁵ Numerical solutions of actual, continuous physical phenomena contain errors, or uncertainties, due to temporal
¹⁹⁶ and spatial discretisation. Reliance on the numerical method of investigation puts the responsibility on the user to
¹⁹⁷ minimise and justify the magnitude of error introduced in the solution.

¹⁹⁸ While CFD users usually point towards their low Courant-Friedrichs-Lowy number to substantiate their claim of
¹⁹⁹ temporal convergence for their numerical solutions, researchers demonstrate the spatial convergence of their solution
²⁰⁰ through either one of these methods. First, by solving the governing equations on several grids, each grid being a
²⁰¹ finer version of the previous one and showing that the quantities of interest are approximately the constant on all grids
²⁰² tested. One then chooses the mesh with a medium resolution to use in the subsequent data collection (Wu, 2011; Ding
²⁰³ et al., 2013, 2015a, 2019).

²⁰⁴ **3.2. Grid independency study via Richardson extrapolation and grid convergence index**

²⁰⁵ Like the first, the second method solves the governing equations on successively finer grids. However, instead of
²⁰⁶ arguing that one obtains similar results on all the grids, the investigator checks whether the quantities of interest tend
²⁰⁷ towards value, as one solves the governing equation on successively finer grid resolutions (Richardson and Gaunt, 1927;
²⁰⁸ Stern et al., 2001). This method, of checking for convergence pays attention not only on the presumed converged value
²⁰⁹ but also on the trend of convergence. Literature that employ this method impose a monotonic convergence condition
²¹⁰ (Stern et al., 2001; Mat Ali et al., 2011; Ali et al., 2012; Maruai et al., 2018) on their quantities of interest, adding an
²¹¹ extra layer of confidence in the final form of their spatial discretisation.

²¹² Additionally, this method allows for a quantitative description of the degree of convergence through the grid conver-
²¹³ gence index (GCI). Let $f_1, f_2, f_3, \dots, f_k$ denote the quantity of interest obtained from several grids. A larger subscript
²¹⁴ indicates a coarser grid, thus, f_1 denotes the finest while f_k denotes the coarsest grid. Let the difference between
²¹⁵ successive solutions be $\epsilon_{2,1}, \epsilon_{3,2}, \epsilon_{4,3}, \dots, \epsilon_{n,n-1}$, where $\epsilon_{2,1} = f_2 - f_1$, $\epsilon_{3,2} = f_3 - f_2$ and so on. Then, the GCI is
²¹⁶ defined as

$$\text{GCI}_{i+1,i} = F_s \frac{|\epsilon_{i+1,i}|}{f_i (r^p - 1)} \times 100\%, \quad (15)$$

²¹⁷ where F_s , f_i and r^p denotes the safety factor ($= 1.25$), quantity of interest and the refinement ratio, r , between successive
²¹⁸ grids raised to the order of accuracy of the series of solution, p . We refer the reader to Stern et al. (2001); Langley
²¹⁹ Research Centre (2018) for a more detailed discussion on r^p .

220 We can estimate what the solution approaches as the grid size approaches zero by using the p^{th} method. Briefly,
 221 we compute the generalised Richardson extrapolation of the quantity of interest as follows.

$$f_{\text{RE}} = f_1 + \frac{f_1 - f_2}{r^p - 1}, \quad (16)$$

222 where f_{RE} is the Richardson extrapolation of the quantity of interest. Using f_{RE} to estimate the limit of the monoton-
 223ically convergent series of f_i , we can determine the percentage difference of our solution on our finest grid from this
 224 limit as

$$E_i = \frac{f_i - f_{\text{RE}}}{f_{\text{RE}}} \times 100\%. \quad (17)$$

225 Table 2 summarises the result of our grid independency study for the SVIV reduced velocity of $U^* = 22.7$.
 226 We identified three quantities central to the investigation of fluid-structure phenomena, especially the flow-induced
 227 vibration of a circular cylinder. They are the vibration amplitude, vibration frequency and lift coefficient of the cylinder.
 228 We solve the governing equations on three grids which are numbered 1 for the finest, 2 for the medium and 3 for the
 229 coarsest, shown in Fig. 6. If we let v_i be the volume of the i^{th} cell in the grid and N be the total number of cells in the
 230 domain, then, the average cell size is

$$h = \frac{1}{N} \left[\sum_{i=1}^N v_i \right]^{1/3}, \quad (18)$$

231 and the normalised average cell size is hence

$$h/D = \frac{1}{ND} \left[\sum_{i=1}^N v_i \right]^{1/3}. \quad (19)$$

232 Both y_{RMS}^* and Cl_{RMS} starts at an initial value smaller than their Richardson extrapolations, f_{RE} , before approaching
 233 it as we decrease the average cell size, h . This similar trend can perhaps be attributed to the causal relationship between
 234 the lift coefficient and vibration amplitude. The lift drives and sustains the vibration, hence a small lift produces a small
 235 vibration, and when the lift amplitude becomes higher, so too does the vibration amplitude. The vibration frequency,
 236 on the other hand, starts at a value larger than its f_{RE} before approaching f_{RE} .

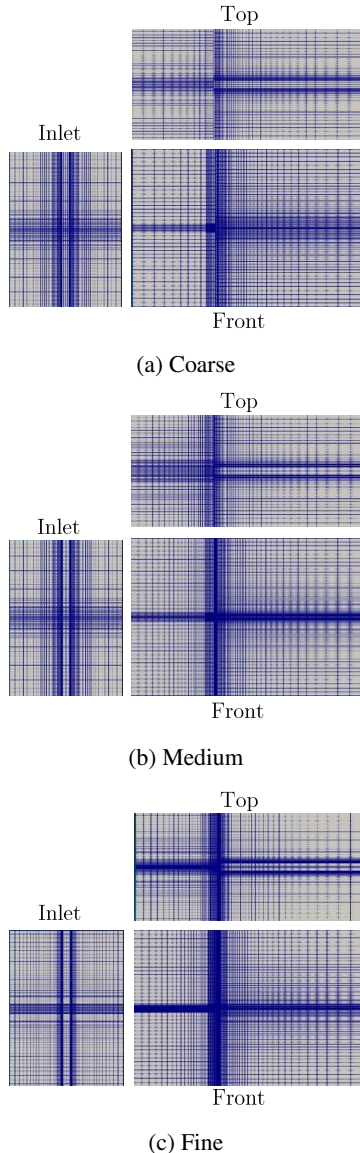


Figure 6: Three meshes used in the grid convergence study. Figures 6a, 6b and 6c show the coarse, medium and fine meshes viewed perpendicular to three main viewing positions: from the inlet, the top and the front, which is looking directly at the cylinder end.

The quantity Cl_{RMS} experiences the most significant drop in GCI as we refine the grid. The GCI is close to one-third (30.92%) as we refine the grid from coarse to medium with a refinement ratio of 1.376. The refinement ratio is calculated by dividing the number of cells in one grid with the next one down the refinement line. Following the grid numbering convention explained previously, dividing the number of cells in the fine grid (grid 1) with the number of cells in the medium grid (grid 2) gives us the refinement ratio from medium to fine, or $r_{2,1}$. Similarly, dividing the number of cells in the medium grid (grid 2) with the number of cells in the coarse grid (grid 3) gives us the refinement

243 ratio from coarse to medium, or $r_{3,2}$. We can generalise this to i -number of grids as follows.

$$r_{i+1,i} = \frac{S_{\text{grid},i+1}}{S_{\text{grid},i}}, \quad (20)$$

244 where $S_{\text{grid},i}$ denotes the total number of cells in the i^{th} grid. The GCI of Cl_{RMS} drops further to 1.63% as the mesh is
245 refined more with a refinement ratio of 1.304.

246 The GCI for y_{RMS}^* also drops by one order of magnitude as can be seen by comparing $\text{GCI}_{3,2}$ with $\text{GCI}_{2,1}$. Again,
247 this similar trend of improvement points to the causal relationship between lift and displacement of the cylinder. The
248 GCI for f^* , however, drops by approximately a factor of 6 instead of one order of magnitude, unlike the GCIs of y_{RMS}^*
249 and Cl_{RMS} .

Table 2
Summary of grid independency study.

Parameter/ metric	Cl_{RMS}	$y_{\text{RMS}}^* = y^*/D$	$f^* = f_{\text{cyl.}}/f_n$
f_{RE}	0.262	0.369	0.969
f_1	0.2598	0.3687	0.9695
f_2	0.2430	0.3588	0.9740
f_3	0.0805	0.2374	1.0220
$ \epsilon_{2,1} $	0.02	0.01	0.004
$ \epsilon_{2,1} $	0.16	0.12	0.48
$R = \epsilon_{2,1} / \epsilon_{2,1} $	0.10	0.08	0.094
$\text{GCI}_{3,2}$	30.92	6.00	0.64
$\text{GCI}_{3,2}$	1.63	0.52	0.10

250 We provide visual representations of the convergent Cl_{RMS} , y_{RMS}^* and f^* series in Figs. 7, 8 and 9. Note how the
251 quantity of interest is very close to its Richardson extrapolation at the fine grid (grid 1) for all Cl_{RMS} , y_{RMS}^* and f^* .
252 This implies that the fine grid already provides adequate spatial discretisation for the problem we are studying, and
253 further refinements, while able to nudge our solutions even closer to the limit that is the Richardson extrapolation, may
254 not be optimal in terms of usage of computational resources. Values of y_{RMS}^* and f^* at the fine grid already fall within
255 experimental uncertainty as evidenced by our measurement in §2.4 and the work by Koide et al. (2013). Hence, all
256 succeeding numerical data are gathered from the fine grid.

257 4. Single plate amplitude and frequency response

258 4.1. Amplitude response

259 We compared our experiment and numerical results with those from Koide et al. (2013) and Nguyen et al. (2012) in
260 Fig. 10. Figure 10a shows the amplitude response of our single plate experiment and simulation. We use the root-mean-
261 square value of the cylinder displacement to represent the amplitude responses instead of the maximum displacement.

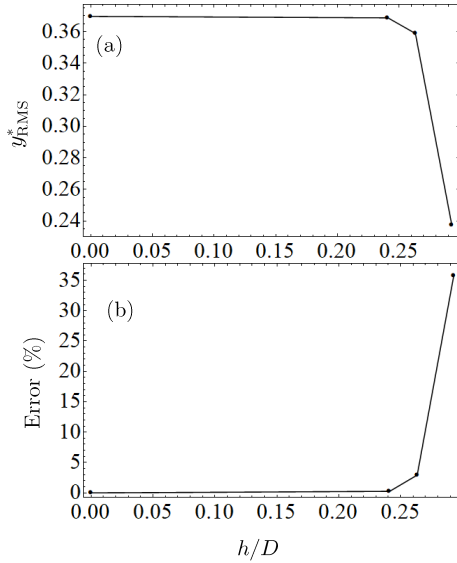


Figure 7: The convergence diagram for y_{RMS}^* . Figure 7a shows how y_{RMS}^* converges close to the Richardson extrapolation value while Fig. 7b shows how the error (difference between the value obtained from a particular mesh and the Richardson extrapolation) decreases with decreasing grid spacing.

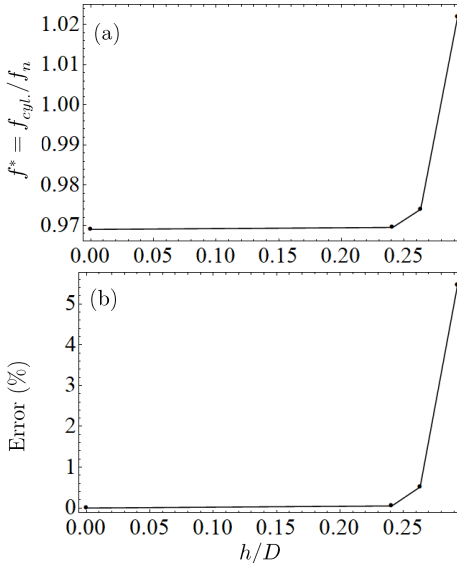


Figure 8: The convergence diagram for f^* . Figure 8a shows how f^* converges close to the Richardson extrapolation value while Fig. 8b shows how the error (difference between the value obtained from a particular mesh and the Richardson extrapolation) decreases with decreasing grid spacing.

262 The reason for this is twofold: first, using y_{RMS}^* facilitates comparison of data with Nguyen et al. (2012) and Koide
 263 et al. (2013), who also used y_{RMS}^* in their work. Second, because the cylinder displacement is an intermediate quantity
 264 for the estimation of harnessed power (Maruai et al., 2017, 2018), and the usage of root-mean-square amplitude of
 265 cylinder displacement gives a direct preview of mean harnessed power.

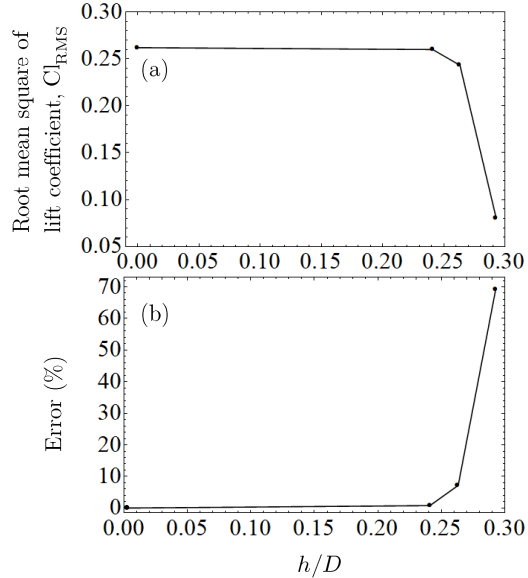


Figure 9: The convergence diagram for Cl_{RMS} . Figure 9a shows how Cl_{RMS} converges close to the Richardson extrapolation value while Fig. 9b shows how the error (difference between the value obtained from a particular mesh and the Richardson extrapolation) decreases with decreasing grid spacing.

266 There is virtually no vibration for both our experiment and simulation when $U^* \leq 18.2$, except for a small peak
 267 at $U^* = 6.8$. We attribute this peak to the upper branch of KVIV, which still exists, although suppressed due to the
 268 cruciform configuration of the system (Shirakashi et al., 1989; Nguyen et al., 2012). However, when U^* exceeds 18.2,
 269 we observe a sudden jump in U^* right up to about 0.4, for both our experiment and simulation. This we attribute to
 270 the formation of the streamwise vortices that drive SVIV.

271 After the inception of SVIV, the value for y_{RMS}^* drops down to approximately 0.3, before recovering to a value
 272 that is close to what was observed by Nguyen et al. (2012) and Koide et al. (2013). This sudden jump followed by a
 273 gradual drop and a gradual rise in y_{RMS}^* was not found in the works of Nguyen et al. (2012) nor Koide et al. (2013),
 274 even though their experimental parameters are reasonably close to what we use in both our experiment and simulation.

275 We, therefore, attribute this difference to the higher turbulence level set in our work. The turbulence level in the
 276 works of Nguyen et al. (2012), for example, was $< 2.8\%$ throughout their range of Reynolds number. Instead, the
 277 initial turbulence level in our setup, both experimental and numerical, is approximately double that value. Because
 278 of this, the turbulence amplification due to the onset of streamwise vortices (Zhao and Lu, 2018) — especially for a
 279 circular cylinder-strip plate cruciform (Koide et al., 2017) — is also higher compared to the experiments of Nguyen
 280 et al. (2012) and Koide et al. (2013). This higher compound turbulence warps the dominant vortical structure and
 281 introduces an increasing amount of intermittency to the lift signal, and by extension, to the displacement time history
 282 of the cylinder.

283 One can simply inspect the error bars within $18.2 \leq U^* \leq 22.7$ in Fig. 10a to verify the greater sample dispersion

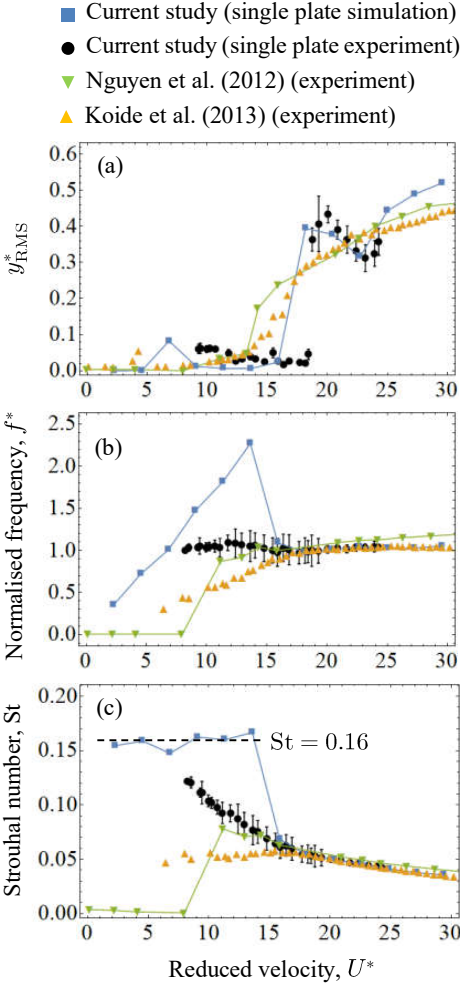


Figure 10: The amplitude and frequency response of our cruciform system, compared with results from Nguyen et al. (2012) and Koide et al. (2013). Figure 10a shows the amplitude response using y_{RMS}^* , Fig. 10b the frequency response using f^* and Fig. 10c also the frequency response, but using the Strouhal number of vibration.

within that range of U^* . This intermittency ultimately vanishes as the dominant vortical structures become sufficiently stable to retain enough periodicity in its formation. Our numerical results also seem to support this argument, as evidenced by the time history of U^* within $18.2 \leq U^* \leq 29.5$ in Fig. 11. There exists a distinct increase in intermittency for the time histories in Fig. 11a, that disappears once $U^* \geq 23$ as can be seen in Fig. 11b.

4.2. Frequency response

Figure 10b compares the frequency responses of our experiment and numerical results with those in Nguyen et al. (2012) and Koide et al. (2013). We use the normalised frequency f^* in Fig. 10b and the vibration Strouhal number in Fig. 10c to aid comparison between the results. In our experiments, the value for f^* always fall close to unity. However, if we inspect the size of the error bars, we observed a range of U^* where there exists a higher degree of variance in

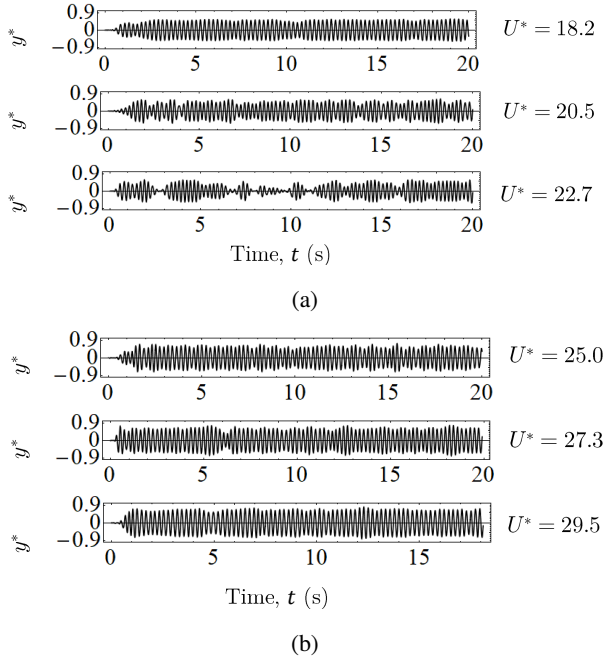


Figure 11: The time series of cylinder displacement between $18.2 \leq U^* \leq 29.5$. Fig. 11a groups the cylinder displacement signal between $18.2 \leq U^* \leq 22.7$, where there seems to be an increase in intermittency in the displacement signal, while Fig. 11b groups the cylinder displacement signal between $25.0 \leq U^* \leq 29.5$, where the intermittency in the displacement signal vanishes.

293 the sample measurements between $13.6 \leq U^* \leq 20.5$. The reason for this lies in $13.6 \leq U^* \leq 20.5$ coinciding with
 294 the desynchronization region of the KVIV regime up to $U^* = 18.2$, and then overlaps with the intermittent vibration
 295 of SVIV up to $U^* = 20.5$. Within these two regimes, the cylinder displacement time history – from which f^* is
 296 calculated – varies considerably in amplitude and periodicity, resulting in larger error bars. In Fig. 10c we can see the
 297 overall trend being more similar to the results of Koide et al. (2013) rather than Nguyen et al. (2012), which is likely
 298 due to a higher similarity between our experimental setup with that of Koide et al. (2013), most striking in terms of
 299 the gap ratio $G = g/D$, which is identical.

300 Our numerical results exhibit a significantly different trend, but only up to $U^* = 15.9$. We observe in Fig. 10b that
 301 the vibration frequency of the cylinder increases linearly, even past $U^* = 6.8$, which is the upper branch of the KVIV
 302 regime. Converting f^* into Strouhal number reveals that the cylinder is vibrating close to the Karman frequency of
 303 the system. The Karman frequency of a smooth, fixed circular cylinder refers to the shedding frequency of Karman
 304 vortices in its wake. An empirical relationship with Reynolds number exists for $250 < \text{Re} < 2 \times 10^5$, which is the
 305 following (Blevins, 1990).

$$\text{St} = 0.198 \left(1 - \frac{19.7}{\text{Re}} \right) \quad (21)$$

306 The values we get using Eq. 21 are nearly constant about 0.19 for $U^* \leq 13.6$. The slight discrepancy from our
 307 Strouhal number mean (≈ 0.16) in the $U^* \leq 13.6$ range can be ascribed to us studying a cruciform structure instead
 308 of the smooth circular cylinder upon which Eq. 21 was originally based (Blevins, 1990).

309 The discrepancies found especially in Fig. 10b most probably stem from the same reasons explained by Nguyen
 310 et al. (2012). The lowest y_{RMS}^* recorded in our simulation within $6.8 \leq U^* \leq 13.6$ was in the order of 10^{-5} m (10
 311 microns). A numerical study has no problem recording vibration of this order as the precision of the numerical solution
 312 is only limited by the processor architecture. Experimental work, however, requires not only the sensitivity but also
 313 the isolation from the background noise that forces the cylinder to vibrate close to the natural frequency of the system
 314 f_n (Nguyen et al., 2012), which consequently overpowers this minimal amplitude vibration. Once streamwise vortices
 315 form, however, their shedding and cylinder vibration synchronises close to f_n , thus locking the normalised vibration
 316 frequency back to $f^* \approx 1$.

317 5. Temporal evolution of the lift coefficient

318 5.1. Ensemble empirical mode decomposition and Hilbert transform

319 To obtain a clearer picture of the temporal characteristics of the lift and cylinder displacement signals, we decided
 320 to employ the ensemble empirical mode decomposition (EEMD) method (Huang et al., 1998; Wu and Huang, 2008)
 321 on the signals, and compute their instantaneous phase lag, frequency and amplitude using the Hilbert transform.

322 The Hilbert transform (HT) has been used in the past to study the instantaneous phase and frequencies of KVIV
 323 (Khalak and Williamson, 1999). However, the signal must be monochromatic if we are to obtain a physically mean-
 324 ingful result after applying HT. EEMD is a way to pre-process the signal and get components that (1) have zero mean,
 325 and (2) have an equal number of extrema and zero crossings, or they differ only by one. Functions that fulfil these
 326 criteria are called intrinsic mode functions (IMF), and they guarantee a physically meaningful result to HT (Gumelar
 327 et al., 2019; Zhou et al., 2019). Unlike Fourier transform, which is an analytical method of signal decomposition based
 328 on circular functions in the complex plane, EEMD is algorithmic, and the processes undertaken can be summarised as
 329 follows.

330 Produce 150 white noise signals of length equal to the original signal and amplitude equal to 0.2 of the standard
 331 deviation of the original signal. Then, add to the set of white noises the original signal – creating 150 variations of
 332 the original signal. Following that, we apply the empirical mode decomposition (EMD) algorithm on each of the 150
 333 signals. The EMD algorithm is summarised below.

- 334 1. Construct the envelope of the signal by connecting all maxima/minima with cubic splines.
- 335 2. Find the local mean of the envelope for the span of the data.
- 336 3. Find the difference between the local mean and the original data.

³³⁷ 4. Repeat steps 1 and 2 on the difference in 3 for ten times (Wu and Huang, 2008).

³³⁸ The steps above produce a set of intrinsic mode functions or IMFs for each of the 150 variations of the original
³³⁹ signal. Then, we average the first IMF component from each of the decomposed original signal variations, to obtain
³⁴⁰ the first EEMD IMF, C_1 , of the original signal. We do the same for the second, third, until the i^{th} component for each
³⁴¹ of the 150 original signal variations, thus obtaining C_2, C_3, \dots, C_i .

³⁴² To compute the phase lag between the characteristic IMFs of the lift coefficient and normalised cylinder displace-
³⁴³ ment, we select the IMF components with the highest correlation to the y^* signal at that particular U^* , to represent the
³⁴⁴ signals, denoted as C_{y^*,y^*} for the characteristic normalised cylinder displacement, and C_{Cl,y^*} as the characteristic lift
³⁴⁵ coefficient signal. The phase lag, instantaneous frequency and instantaneous amplitude of the signal is subsequently
³⁴⁶ computed by constructing an analytical signal $z(t)$ from C_1, C_2, \dots, C_i by computing the Hilbert transform of the IMF,
³⁴⁷ H_i ,

$$H_i(t) = \frac{1}{\pi} \text{PV} \int_{-\infty}^{\infty} \frac{C_i(\tau)}{t - \tau} d\tau, \quad (22)$$

where PV denotes the Cauchy principal value, and then constructing the analytical signal as follows.

$$z(t) = C_i(t) + iH_i(t) \quad (23)$$

³⁴⁸ Note that i in Eq. 23 is the complex number.

³⁴⁹ We refer the reader interested in the details of EEMD and Hilbert transform, also collectively known as the Hilbert-
³⁵⁰ Huang transform (HHT), to the following excellent texts on the subject (Huang and Attoh-Okine, 2005; Huang, 2014).

³⁵¹ 5.2. The KVIV regime ($U^* \leq 13.6$)

³⁵² At reduced velocities $U^* = 2.3$ and 4.5 , the phase lags ϕ (deg.) between Cl and U^* are practically zero throughout
³⁵³ the whole observation time. The characteristic IMFs of Cl and y^* at $U^* = 4.5$ exemplifies this trend, as showcased in
³⁵⁴ Fig. 12. Here, Fig. 12a shows the temporal evolution of C_{y^*,y^*} and C_{Cl,y^*} , which are the characteristic IMFs of y^* and
³⁵⁵ Cl, respectively. Figure 12b shows the phase lag between C_{y^*,y^*} and C_{Cl,y^*} , and Fig. 12c presents the HHT spectrogram
³⁵⁶ of Cl. The HHT spectrogram visualises the instantaneous frequency and amplitude of the IMF components of Cl. The
³⁵⁷ trend that one notices in Fig. 12b is similar to what was observed in Khalak and Williamson (1999), a study that also
³⁵⁸ employs the Hilbert transform to obtain the instantaneous phase, albeit without EEMD. The dominant IMF component
³⁵⁹ (IMF component sustaining the highest amplitude throughout the whole observation time) of the lift coefficient has a
³⁶⁰ normalised frequency $f_{Cl}^* = f_{Cl}/f_n$ (Fig. 12c) centred at approximately $f_{Cl}^* = 0.75$.

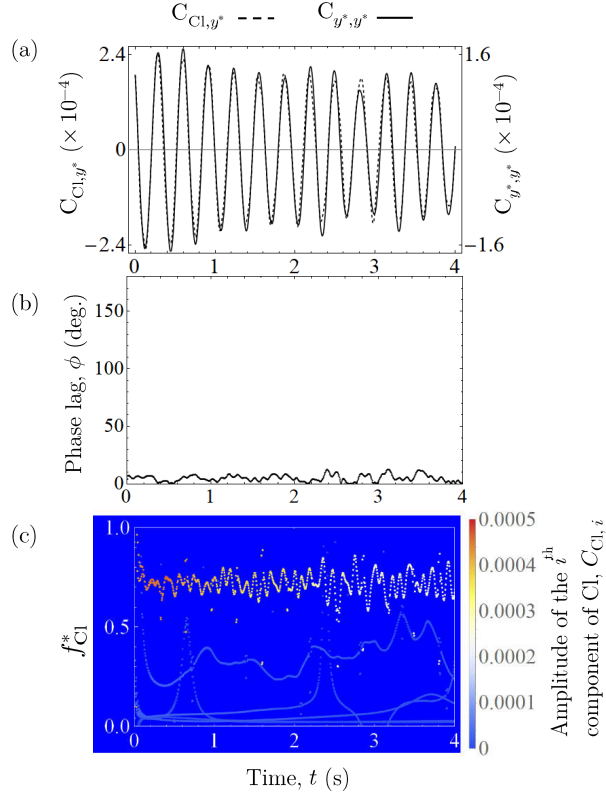


Figure 12: Temporal analysis of the lift coefficient and normalised cylinder displacement signal at $U^* = 4.5$. We show C_{Cl,y^*} and C_{y^*,y^*} side by side in Fig. 12a, present the temporal evolution of the phase lag ϕ in Fig. 12b and show the temporal evolution of the instantaneous frequency of the lift coefficient signal in Fig. 12c.

Once we enter the upper branch of KVIV at $U^* = 6.8$, ϕ jumps to approximately 110 deg. This jump in ϕ is characteristic of the transition to the upper branches as also observed by Maruai et al. (2018), among others. Both C_{Cl,y^*} and C_{y^*,y^*} signals are visibly very periodic, and the dominant frequency band of Cl, is centred at ≈ 1 , as one can verify in Fig. 13c.

As we increase U^* even further up to $U^* = 13.6$, we see a similar trend for all $U^* = 9.1, 11.4, 13.6$ examined: C_{y^*,y^*} and C_{Cl,y^*} are both qualitatively very periodic. Their phase lags are very close to 180 deg., and the dominant Cl frequency bands exhibit a time-averaged value that increases linearly with respect to U^* , in a manner that the Strouhal number of Cl is always ≈ 0.16 on average. We present the representative case of $U^* = 13.6$ in Fig. 14. Note how ϕ in this range of U^* varies much less with respect to time, compared to ϕ at $U^* = 6.8$, and the dominant frequency band of Cl is much narrower compared to the dominant frequency band at $U^* = 6.8$, indicating a highly periodic and self-similar oscillation of lift.

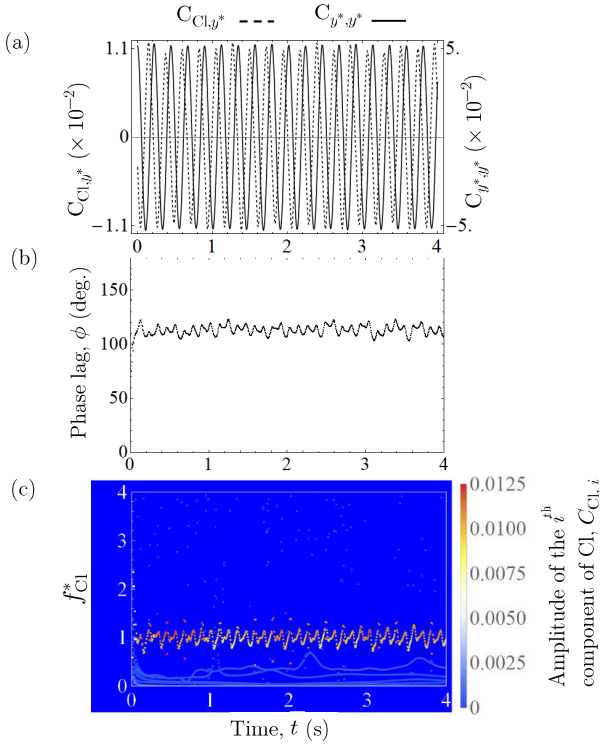


Figure 13: Temporal analysis of the lift coefficient and normalised cylinder displacement signal at $U^* = 6.8$. We show C_{Cl,y^*} and C_{y^*,y^*} side by side in Fig. 13a, present the temporal evolution of the phase lag ϕ in Fig. 13b and show the temporal evolution of the instantaneous frequency of the lift coefficient signal in Fig. 13c.

372 5.3. Transition to SVIV ($15.9 \leq U^* \leq 18.2$)

373 Previously in the $U^* \leq 13.6$ range, we observed that the temporal profile of both Cl and y^* are very similar to each
 374 other, except that Cl leads y^* by a certain amount. This similarity in profile supports the assertion that the vibration
 375 within $U^* \leq 13.6$ is driven exclusively by the shedding of Karman vortices, which brings the onset of the alternating
 376 lift. Analogously, one might expect a similar profile between Cl and y^* when streamwise vortices drive the vibration.
 377 However, this does not seem to be the case.

378 Once we reach $U^* = 15.9$, we observe that it has become difficult to argue that the profile of y^* is just a lagged
 379 version of the profile of Cl. This is shown in Fig. 15a, with the enlarged version in Fig. 15b. The profile of Cl looks
 380 like the result of several signals in superposition, which one can almost distinguish from the presence of two types of
 381 maxima at two different amplitude heights. We put a red dashed line and a red dashed-dot line in Fig. 15b as visual cues
 382 indicating the two amplitude heights. Decomposing the lift coefficient signal using EEMD reveals partial evidence
 383 supporting the compound signal hypothesis.

384 Once we have decomposed the signal using EEMD, we replot Fig. 15a using C_{Cl,y^*} and C_{y^*,y^*} in Fig. 16a. One can
 385 clearly see that the part of Cl signal responsible for driving the vibration at $U^* = 15.9$ is embedded in the original Cl

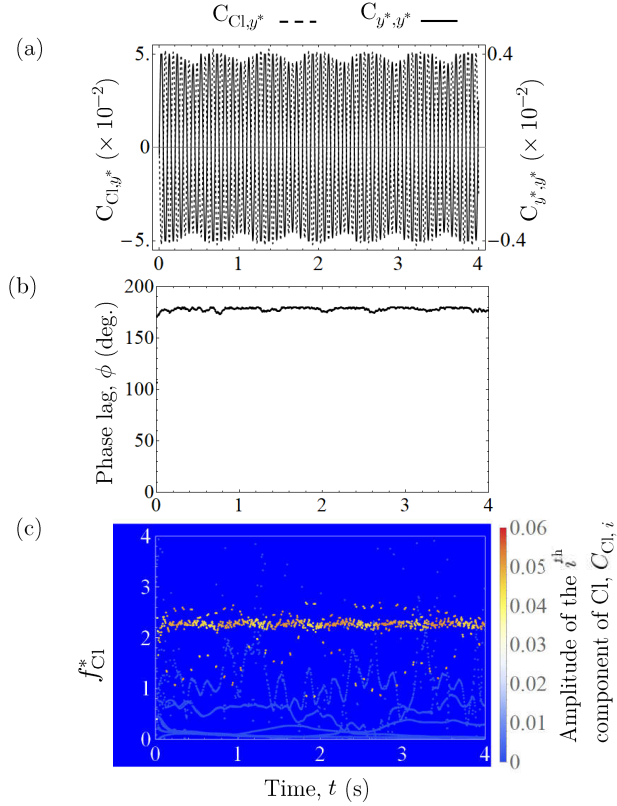


Figure 14: Temporal analysis of the lift coefficient and normalised cylinder displacement signal at $U^* = 13.6$. We show C_{Cl,y^*} and C_{y^*,y^*} side by side in Fig. 14a, present the temporal evolution of the phase lag ϕ in Fig. 14b and show the temporal evolution of the instantaneous frequency of the lift coefficient signal in Fig. 14c.

signal (Fig. 16a), and decomposition via EEMD managed to recover this signal, which leads C_{y^*,y^*} by approximately 150 deg. on average, throughout the whole observation time (Fig. 16b). This decline from $\phi \approx 180$ deg. at reduced velocities $9.1 \leq U^* \leq 13.6$, to $\phi \approx 150$ deg. at $U^* = 15.9$ is quite sizeable, suggesting a fundamental change in flow dynamics, particularly in terms of vortical structure. Another notable change is the increased temporal variation in ϕ from its time-averaged value, in contrast to the evolution of ϕ in the range $9.1 \leq U^* \leq 13.6$, which has very little jitter throughout the observation time.

Inspecting the HHT spectrogram in Fig. 16c reveals two dominant bands in the frequency domain. The first one, marked with a white continuous rectangular box, is the instantaneous frequency for the IMF component of lift shown in Fig. 16a, and its mean frequency lies close to the natural frequency of the system ($f_{Cl}^* \approx 1$). There is; however, a second band of the frequency with nearly similar amplitude around $f_{Cl}^* \approx 3.3$, marked with a white dashed rectangular box. Computing the Strouhal number from this frequency returns a value of $St = 0.20$, which is very close to the Strouhal number for Karman vortices as predicted by Eq. 21 at the Reynolds number equivalent to $U^* = 15.9$, which is $Re = 7.9 \times 10^3$. We thus attribute this second band of frequency as being the footprint left by the shedding of

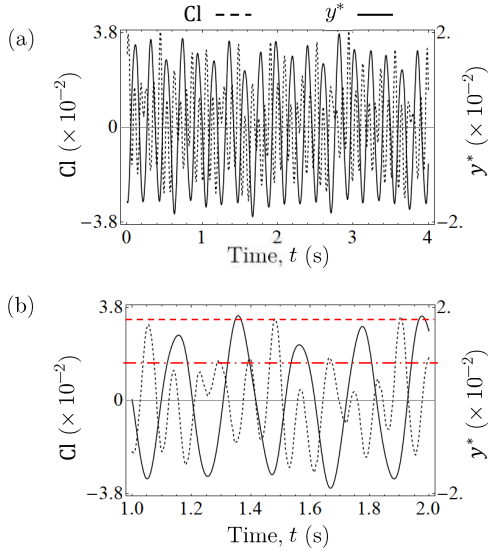


Figure 15: Temporal evolution of y^* and Cl at $U^*15.9$. Figure 15b shows an enlarged view of Fig. 15a. We can barely spot semblance of two signals with different amplitudes superimposed in the Cl signal in Fig. 15b.

399 Karman vortices, and the first band as the result of streamwise vortex shedding. Through visual inspection of Fig. 16c,
 400 both of these dominant frequency bands are markedly wider and the individual values are more scattered from their
 401 time-averaged values than any of their counterparts within $U^* \leq 13.6$.

402 The knowledge that Karman vortices continue to exist and shed from a cruciform structure during SVIV is not
 403 new in the literature. However, this is the first time the lift signal from a cruciform structure undergoing SVIV has
 404 been subjected to EEMD, revealing the signature of the two dominant vortical structures regulating the flow around
 405 the cruciform. Although the amplitude size of the instantaneous frequency band due to Karman vortex is comparable
 406 to the streamwise vortex, the reason why the cylinder resists locking into its frequency is perhaps that its frequency too
 407 distant from the natural frequency of the system f_n . The shedding frequency of the streamwise vortex is much closer
 408 to f_n and is thus preferred by the cylinder.

409 We consider the transition to SVIV to be complete at $U^* = 18.2$, when the time-averaged phase lag drops further
 410 to ≈ 20 deg. Figure 17a and 17b documents this observation. The instantaneous phase lag is observed to slip through
 411 360 deg. a little past the two second (2 s) time stamp. By inspecting Fig. 17a, we found that a little past 2 s is
 412 when distortions in the periodicity of C_{Cl,y^*} occur. The slipping through 360 deg. was also observed by Khalak and
 413 Williamson (1999) in their work on KVIV, highlighting the quasi-periodic nature of the signal being analysed. There,
 414 the slip appeared in Khalak and Williamson (1999) at the initial branch of KVIV. The overall low value of ϕ (≈ 20 deg.
 415 for the whole observation time at $U^* = 18.2$), coupled with the presence of ϕ slippage are suggestive of the possibility
 416 for $U^* = 18.2$ being the initial branch of SVIV.

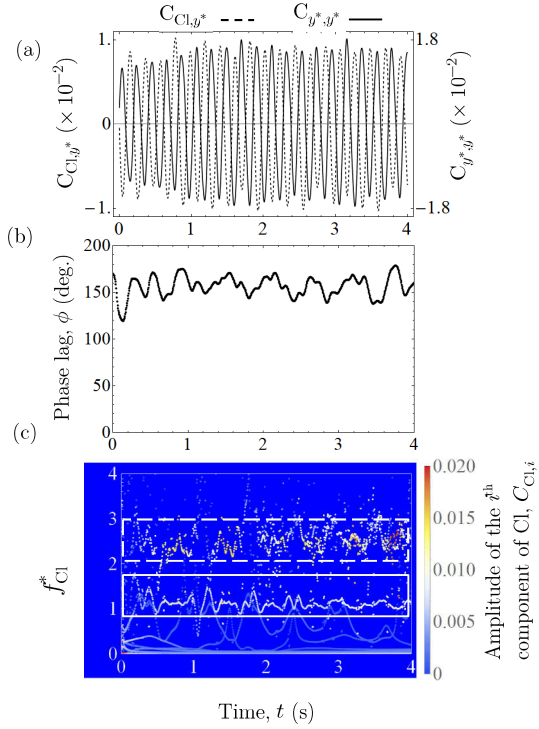


Figure 16: Temporal analysis of the lift coefficient and normalised cylinder displacement signal at $U^* = 15.9$. We show C_{Cl,y^*} and C_{y^*,y^*} side by side in Fig. 16a, present the temporal evolution of the phase lag ϕ in Fig. 16b and show the temporal evolution of the instantaneous frequency of Cl in Fig. 16c.

417 5.4. The stable SVIV regime ($U^* \geq 20.5$)

418 As U^* is increased to 20.5, we can see a jump in ϕ from a mean value of approximately 20 deg. to about 120 deg.,
 419 shown in Fig. 18a. The phase slippage discussed previously is also observed, indicating the quasi-periodic nature
 420 of the lift coefficient signal at this U^* . Incidentally, this quasi-periodicity seems to be the norm for the lift signals
 421 up to $U^* = 27.3$, as suggested by the phase slippages evident in Figs. 18b, c and d. The slippage only stops once
 422 U^* reaches 29.5, suggesting a more periodic behaviour of the lift coefficient compared to its counterparts between
 423 $20.5 \leq U^* \leq 27.3$. Although the instantaneous phase between $20.5 \leq U^* \leq 27.3$ implies a quasi-periodic nature,
 424 their time-averaged values at each U^* are contained in the narrow region $114 < \phi$ (deg.) < 135 , as is the value for
 425 ϕ at $U^* = 29.5$. This observation that the time-averaged value of ϕ to only slowly vary with respect to U^* , once U^*
 426 increases past 20.5, can be interpreted as the dominant flow structures settling into a stable form that becomes more
 427 resilient against external excitations. Based on this feature, we classified $20.5 \leq U^* \leq 29.5$ as the upper branch of
 428 SVIV.

429 The data on the evolution of ϕ allows us to construct a map of the “branches” of vibration modes observed in the
 430 range of U^* that we studied. As the branches are mapped against U^* , we need a representative value of ϕ at each
 431 U^* . To achieve this, we took the time-averaged values of ϕ , i.e. ϕ_{mean} , and plotted them against U^* in Fig. 19. The

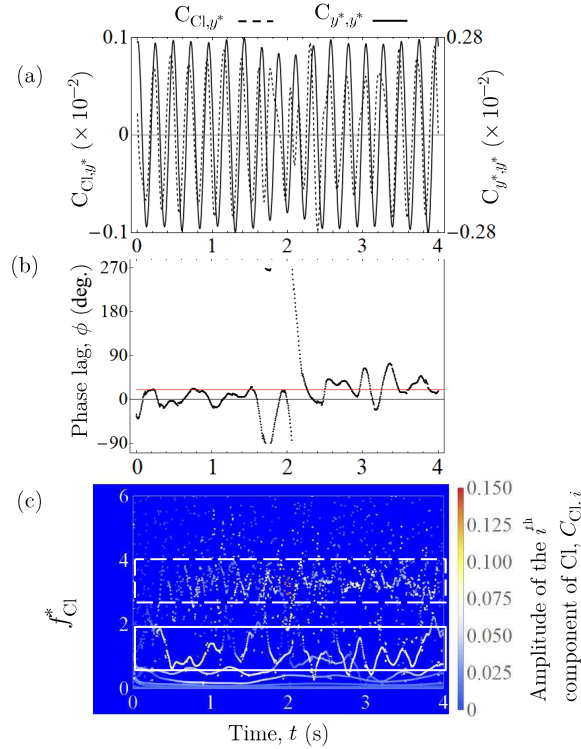


Figure 17: Temporal analysis of the lift coefficient and normalised cylinder displacement signal at $U^* = 18.2$. We show C_{Cl,y^*} and C_{y^*,y^*} side by side in Fig. 17a, present the temporal evolution of the phase lag ϕ in Fig. 17b and show the temporal evolution of the instantaneous frequency of Cl in Fig. 17c.

region A indicates the initial branch of KVIV, where ϕ_{mean} is close to zero. Region B denotes the upper/lower branch of KVIV, where the system experiences a jump from $\phi_{\text{mean}} \approx 0$ to greater than 110 deg. The value of ϕ_{mean} settles very close to 180 deg. towards the end of this upper/lower branch.

Then, ϕ_{mean} experiences a slight drop from about one-sixth the value of ϕ_{mean} in region B, as we enter region C, marking the start of the transition to the SVIV regime. Following this, the system undergoes a more sudden drop to $\phi_{\text{mean}} \approx 20$ deg. at $U^* = 18.2$. This we designate as region D. Finally, in region E, we observe another jump in ϕ_{mean} from $\phi_{\text{mean}} \approx 20$ deg. in region D to approximately 120 deg. when $U^* \geq 20.5$.

6. Estimation of harnessable power

6.1. Mathematical model for power estimation

The mathematical model for harnessable power estimation in this study follows that which had been derived in Raghavan et al. (2007). In these works, the authors mentioned that work done by the oscillating cylinder W_{cyl} during

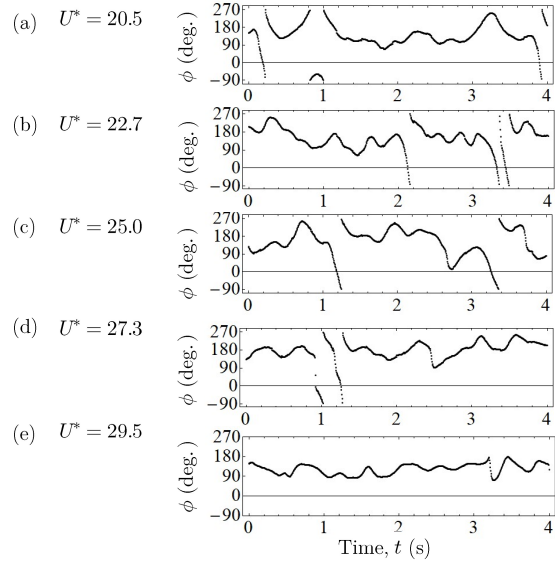


Figure 18: The instantaneous phase lag ϕ of C_{Cl,y^*} in the range $20.5 \leq U^* \leq 29.5$. We can observe ϕ slipping through 360 deg. between $20.5 \leq U^* \leq 27.3$, before disappearing at $U^* = 29.5$; an indication of improved stability and resilience of the vortical structure driving the vibration.

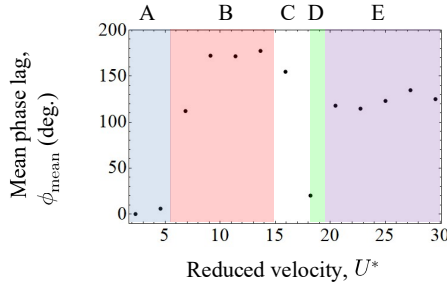


Figure 19: Vibration regimes identified during analysis of ϕ . To capture the evolution of ϕ with respect to U^* , a representative value for ϕ at each U^* must be selected. We chose to use the time-averaged ϕ , ϕ_{mean} , as the representative value.

443 one cycle of oscillation $T_{\text{osc.}}$ is as follows.

$$W_{\text{cyl.}} = \int_0^{T_{\text{osc.}}} (F_L \cdot \dot{y}) dt \quad (24)$$

444 where both the lift F_L and cylinder velocity \dot{y} are both functions of time. Through several manipulations and simplifying
445 assumptions (Sun et al., 2016), the power captured by the system can be written, using our parameters, as the fluid

446 power

$$P_{\text{Fluid,RMS}} = \frac{1}{2} \rho \pi C_{\text{Cl,RMS}} U^2 f_{\text{cyl},y^*} D L \sin(\phi), \quad (25)$$

447 or the mechanical power

$$P_{\text{Mech.,RMS}} = 8\pi^3 m_{\text{eff.}} \zeta_{\text{tot.}} (y_{\text{RMS}}^* f_{\text{cyl.}})^2 f_n. \quad (26)$$

448 Here, $P_{\text{Fluid,RMS}}$, $P_{\text{Mech.,RMS}}$, L , $C_{\text{Cl,RMS}}$, $\zeta_{\text{tot.}}$ and $m_{\text{eff.}}$ are the root-mean-square of fluid power, root-mean-square
 449 of mechanical power, length of the circular cylinder, characteristic root-mean-square of lift amplitude, total damping
 450 coefficient, and the system effective mass respectively. We use C_{Cl,y^*} to represent $C_{\text{Cl,RMS}}$ in Eq. 25. We choose
 451 to use root-mean-square (parameters with subscript RMS) quantities in Eq. 24 instead of the maximum values like
 452 the original authors because that may lead to a misunderstanding that the maximum value is sustained throughout
 453 the observation window. This obviously is not always the case in our study, especially once the system transits into
 454 the SVIV regime. Recall that the time series analysis of $y^*(t)$ and $\text{Cl}(t)$ in §4.1 revealed that there is a degree of
 455 intermittency in both signals that cannot be overlooked at certain ranges of U^* . Using the root-mean-square value
 456 allows us to partially take this into account in the estimation of harnessable power.

457 Figure 20 shows the comparison between power estimated from our experiment and numerical results, with the
 458 experimental results of Nguyen et al. (2012) and the direct power measurement of Koide et al. (2013). Only the value
 459 for $P_{\text{Mech.,RMS}}$ is computed from our experimental results due to the absence of lift data. Our numerical results have
 460 both lift and cylinder displacement data, and hence, we calculated both $P_{\text{Fluid,RMS}}$ and $P_{\text{Mech.,RMS}}$. We estimated the
 461 power from the experimental results of Nguyen et al. (2012) by interpolating missing data points in both their amplitude
 462 and frequency responses to compute the value of $P_{\text{Mech.,RMS}}$ at a given value of U^* . The direct power measurement
 463 by Koide et al. (2013) was done by connecting the elastic support of the cylinder to a coil. The coil moves with the
 464 cylinder, thus creating a relative piston motion against a fixed magnet and produces an alternating current.

465 The estimated power in the KVIV regime $U^* \leq 15.9$ produces power only in the order of μW , which is relatively
 466 insignificant in contrast to the magnitude of power produced in the SVIV regime (mW). In the region $18.2 \leq U^* \leq 22.7$,
 467 $P_{\text{Mech.,RMS}}$ for our experiment and numerical work exhibits a similar trend where we observed a sudden jump in power
 468 output, followed by a gradual decrease. This gradual decrease can be attributed to the increased turbulence level right
 469 after the onset of SVIV that imposes a degree of intermittency to the normalised cylinder displacement signal, y^* . For
 470 $P_{\text{Fluid,RMS}}$, however, the quantity exhibits a monotonic increase in the range $18.2 \leq U^* \leq 22.7$. We only observe

- $P_{\text{Mech.,RMS}}$, current study (experiment)
- $P_{\text{Fluid,RMS}}$, current study (numerical)
- $P_{\text{Mech.,RMS}}$, current study (numerical)
- ▶ $P_{\text{Measured,RMS}}$, Koide et al. (2013) (experiment)
- △ $P_{\text{Mech.,RMS}}$, Nguyen et al. (2012) (experiment)

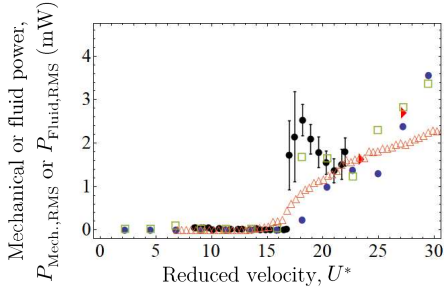


Figure 20: Estimated root-mean-square of mechanical power $P_{\text{Mech.,RMS}}$, fluid power $P_{\text{Fluid,RMS}}$, or both, of our experimental and numerical results, compared with results of similar studies in the literature. The fluid power $P_{\text{Fluid,RMS}}$ is calculated only from the results of our numerical study as the others did not measure lift.

471 a dip in $P_{\text{Fluid,RMS}}$ at $U^* = 25.0$, suggesting an increase in intermittency of C_{Cl,y^*} at this U^* . In the experimental
 472 work of Nguyen et al. (2012), $P_{\text{Mech.,RMS}}$ only experiences a monotonic increase in the region $18.2 \leq U^* \leq 22.7$. This
 473 decidedly different response of the system compared to ours most likely stem from the difference in the actual cruciform
 474 used by Nguyen et al. (2012). They used two circular cylinders of diameter 10 mm as their cruciform, whereas we used
 475 a circular cylinder - strip plate in both our experiments and numerical work. There are no data from the direct power
 476 measurement of Koide et al. (2013) to compare with within $18.2 \leq U^* \leq 22.7$.

477 In the range $25.0 \leq U^* \leq 29.5$, we find a reasonably good agreement between the trend found in all data compared:
 478 they increase monotonically with respect to U^* . Although the value of our $P_{\text{Fluid,RMS}}$ falls quite notably below the value
 479 of $P_{\text{Mech.,RMS}}$ at $U^* = 25.0$, other values of $P_{\text{Fluid,RMS}}$, $P_{\text{Mech.,RMS}}$ from our numerical results and the direct power
 480 measurements by Koide et al. (2013) agree well within $27.3 \leq U^* \leq 29.5$. The only set of power data that consistently
 481 falls quite a distance below the others is the $P_{\text{Mech.,RMS}}$ estimated from the experimental data of Nguyen et al. (2012),
 482 which again, is most probably due to the difference in the actual geometry of the cruciform used in their investigation.

483 6.2. Possibility for increasing fluid power, $P_{\text{Fluid,RMS}}$

484 Recall in Fig. 20 that although $P_{\text{Fluid,RMS}}$ is computed according to Eq. 25, which uses $C_{\text{Cl,RMS}}$ instead of the
 485 actual root-mean-square amplitude of lift (Cl_{RMS}), the resulting power estimate does not result in a trend that is totally
 486 different from the trend found in the other datasets. Furthermore, except for $P_{\text{Mech.,RMS}}$ estimated from the experimental
 487 data of Nguyen et al. (2012), the values of $P_{\text{Fluid,RMS}}$ are in fairly good agreement with other data that it is compared
 488 against at high U^* ($U^* = 27.3$ and 29.5). We see this is an indication that the lift component selected for use in
 489 computation of $P_{\text{Fluid,RMS}}$ is an arguably faithful representation of the force driving the motion of the cylinder. This

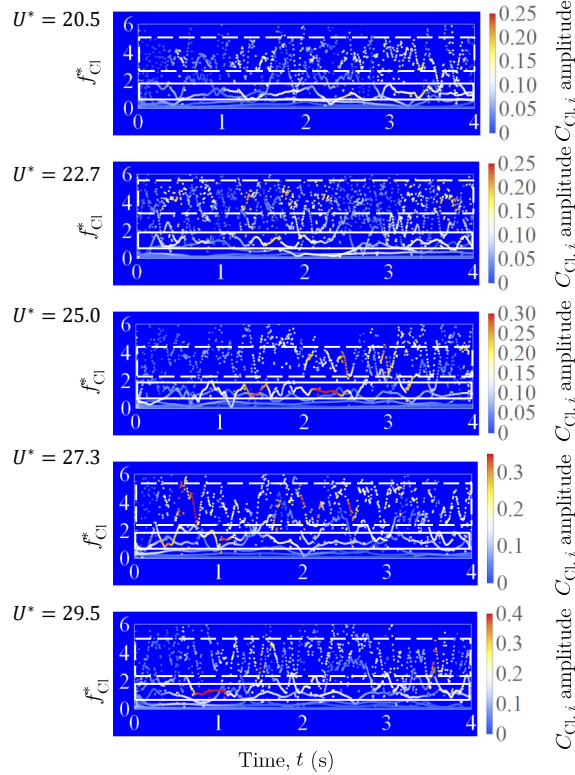


Figure 21: The instantaneous frequency of the lift signal between $20.5 \leq U^* \leq 29.5$. The white, solid boxes enclose the IMF component of CI due to the shedding of the streamwise vortex, while the dashed, white boxes enclose the IMF component due to the shedding of Karman vortex. Through visual inspection, we can see how the degree of dispersion (i.e., height of the box) in the instantaneous frequency of the “Karman component” of lift is about twice that of the “streamwise component” of lift.

suggests that the motion of the cylinder, once it enters the SVIV regime, is driven only by one component, and not the totality, of the lift force. This component – that has a time-averaged frequency close to the natural frequency of the system, f_n – is the “streamwise component” of lift.

Another significant IMF component of the lift force in the SVIV regime is the component whose mean frequency is close to the Karman frequency of vortex shedding, as explained in §5.3. This Karman component of lift has a similar amplitude size as the streamwise component of lift, as evidenced in Fig. 21, and as such is also a dominant component of lift. The Karman components are marked with a dashed, white box, and the streamwise components are marked with a solid, white box, following the convention in Figs. 12, 13, 14, 16 and 17. However, the Karman component fails to affect the cylinder vibration like the streamwise component most probably due to the large difference between the mean frequency of the Karman component and the natural frequency of the system, f_n . The streamwise component has a mean frequency close to f_n and is hence able to synchronise with the vibration of the cylinder, producing a sizeable amplitude response.

Figure 22 shows the root-mean-square amplitude of the Karman and streamwise components of lift in the SVIV

- Karman component ■ Streamwise component

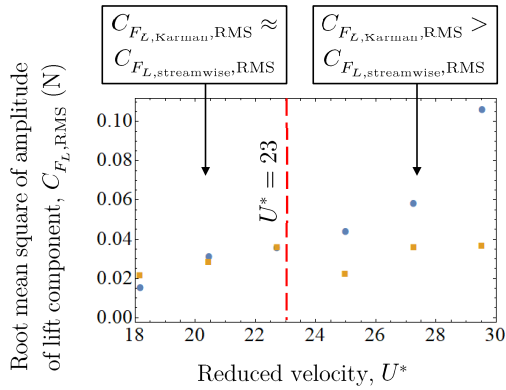


Figure 22: Evolution of the root-mean-square amplitude of two dominant lift components due to Karman ($C_{F_L,\text{Karman,RMS}}$) and streamwise ($C_{F_L,\text{streamwise,RMS}}$) vortices with respect to U^* . The region $18.2 \leq U^* \leq 22.7$ exhibits similar magnitude for both the Karman and streamwise components of lift. On the other hand, the magnitude of amplitude for the Karman component while the region $25.0 \leq U^* \leq 29.5$ is almost always twice that of the streamwise component.

regime $U^* \geq 18.2$. Between $18.2 \leq U^* \leq 22.7$, the magnitude of the Karman and streamwise components are nearly equal. However, once we exceed $U^* = 22.7$, Fig. 22 shows that the contribution to the root-mean-square amplitude of total lift by the Karman component is on average twice the contribution of the streamwise component. Having such a significant contribution towards the root-mean-square amplitude of total lift implies that there is a significant portion of energy from the free stream being used to energise the Karman vortex structure in the flow. Let us assume a hypothetical situation where we can transfer the contribution by the Karman component to the streamwise component of lift. In other words, consider the situation where we can completely redirect the energy from the Karman to the streamwise vortex. Then, the value for $C_{\text{Cl,RMS}}$ in Eq. 25 will increase close to a factor of 2 when $18.2 \leq U^* \leq 22.7$, and close to a factor of 3 when $25.0 \leq U^* \leq 29.5$. This increase in $C_{\text{Cl,RMS}}$ will lead to the scaling of $P_{\text{Fluid,RMS}}$ by the same factor, keeping the other parameters in Eq. 25 constant. This exercise demonstrates the room for improvement possible for $P_{\text{Fluid,RMS}}$ in future developments of cruciform energy harvesters. We shall detail in our future work, a method to modulate the dominant vortical structures to achieve such a goal.

7. Conclusions

In this study, we numerically investigated the temporal evolution of the lift coefficient and cylinder displacement signals of an elastically supported cruciform system in the range $1.1 \times 10^3 < \text{Re} < 14.6 \times 10^3$, or $2.3 < U^* < 29.5$. Our circular cylinder diameter is 10 mm and the natural frequency of the system is 4.4 Hz. Validation of key numerical results was made experimentally in a custom-built open flow channel, using a cruciform system whose parameters were tuned as close as possible to the quantities used in the numerical study. Decomposing the lift coefficient signal in the SVIV regime ($15.9 \leq U^* \leq 29.5$) using EEMD allows us to see that the complexity of the lift coefficient signal as

being caused by the superposition of two dominant components of lift. One due to the shedding of Karman and the other due to the shedding of streamwise vortices. The former has a frequency close to the vortex shedding frequency of Karman vortex from a smooth, isolated circular cylinder, while the latter has a mean frequency close to f_n . Application of the Hilbert-Huang transform on the dominant component of cylinder displacement – and the component of lift most correlated to it – allows for the computation of the instantaneous phase lag between lift and cylinder displacement. The time-averaged phase lag revealed five “branches” of vibration, among which is the initial branch of SVIV at $U^* = 18.2$, which has never been identified before in the literature. We also computed the instantaneous frequency of the lift coefficient, thus revealing the loss of periodicity and self-similarity in the lift coefficient signal as the system enters the SVIV regime. Estimation of power from our results show that the root-mean-square mechanical and fluid power computed from our experimental and numerical work agree to varying degrees depending on U^* with data from similar studies in the literature. Finally, we estimated that the root-mean-square fluid power can potentially be increased close to a factor of 2 within $18.2 \leq U^* \leq 22.7$ and close to a factor of 3 when $25.0 \leq U^* \leq 29.5$. We base this estimation on the premise of redirecting the contribution to the root-mean-square amplitude of total lift from Karman vortex shedding, towards the streamwise component of lift alone.

536 CRediT authorship contribution statement

537 **Ahmad Adzlan:** Conceptualisation, Methodology, Software, Validation, Formal analysis, Investigation, Data cu-
 538 ration, Writing - Original draft preparation, Visualisation. **Mohamed Sukri Mat Ali:** Conceptualisation, Method-
 539 ology, Resources, Writing - Review & Editing, Supervision, Project administration, Funding acquisition. **Sheikh**
 540 **Ahmad Zaki:** Resources, Writing - Review & Editing.

541 References

- 542 Ali, M.S.M., Doolan, C.J., Wheatley, V., 2012. Low Reynolds number flow over a square cylinder with a detached flat plate. International
 543 Journal of Heat and Fluid Flow 36, 133–141. URL: <http://dx.doi.org/10.1016/j.ijheatfluidflow.2012.03.011>, doi:10.1016/j.ijheatfluidflow.2012.03.011.
- 544 Bernitsas, M., Raghavan, K., 2008. Reduction/suppression of VIV of circular cylinders through roughness distribution at $8 \times 10^3 < Re < 1.5 \times 10^5$,
 545 in: Proceedings of the International Conference on Offshore Mechanics and Arctic Engineering - OMAE.
- 546 Bernitsas, M.M., Ben-Simon, Y., Raghavan, K., Garcia, E.M.H., 2009. The VIVACE Converter: Model Tests at High Damping and
 547 Reynolds Number Around 10^5 . Journal of Offshore Mechanics and Arctic Engineering 131. URL: <http://offshoremechanics.asmedigitalcollection.asme.org/article.aspx?articleid=1472649>, doi:10.1115/1.2979796.
- 548 Bernitsas, M.M., Raghavan, K., Ben-Simon, Y., Garcia, E.M.H., 2008. VIVACE (Vortex Induced Vibration Aquatic Clean Energy): A New
 549 Concept in Generation of Clean and Renewable Energy From Fluid Flow. Journal of Offshore Mechanics and Arctic Engineering 130,
 550 041101. URL: <http://www.scopus.com/record/display.url?eid=2-s2.0-56749179917&origin=resultslist&sort=>

Lift Evolution in a Pure Cruciform Energy Harvester

- 553 plf-f{&}src=s{&}st1=A+new+concept+in+generation+of+clean+and+renewable+energy+from+fluid+flow{&}sid=
- 554 620865A71FAF26768C42655E1E8BC194.aXczxbyuHHiXgaIW6Ho7g:230{&}sot=b{&}sdt=b{&}h, doi:10.1115/1.2957913.
- 555 Blevins, R.D., 1990. Flow-induced vibration .
- 556 Deng, J., Ren, A.L., Shao, X.M., 2007. The flow between a stationary cylinder and a downstream elastic cylinder in cruciform arrangement.
- 557 Journal of Fluids and Structures 23, 715–731. URL: <https://www.sciencedirect.com/science/article/pii/S0889974606001472>,
558 doi:10.1016/J.JFLUIDSTRUCTS.2006.11.005.
- 559 Ding, L., Bernitsas, M.M., Kim, E.S., 2013. 2-D URANS vs. experiments of flow induced motions of two circular cylinders in tandem with
- 560 passive turbulence control for 30,000. Ocean Engineering 72, 429–440. URL: <http://www.sciencedirect.com/science/article/pii/S0029801813002448?via%3Dihub>, doi:10.1016/J.OCEANENG.2013.06.005.
- 561 Ding, L., Zhang, L., Kim, E.S., Bernitsas, M.M., 2015a. URANS vs. experiments of flow induced motions of multiple circular cylinders with
- 562 passive turbulence control. Journal of Fluids and Structures 54, 612–628. doi:10.1016/j.jfluidstructs.2015.01.003.
- 563 Ding, L., Zhang, L., Wu, C., Mao, X., Jiang, D., 2015b. Flow induced motion and energy harvesting of bluff bodies with different cross sections.
- 564 Energy Conversion and Management doi:10.1016/j.enconman.2014.12.039.
- 565 Ding, W., Sun, H., Xu, W., Bernitsas, M.M., 2019. Numerical investigation on interactive FIO of two-tandem cylinders for hydrokinetic energy
- 566 harnessing. Ocean Engineering 187, 106215. URL: <https://www.sciencedirect.com/science/article/pii/S0029801819304019>,
567 doi:10.1016/J.OCEANENG.2019.106215.
- 568 Gumerlar, A.B., Purnomo, M.H., Yuniarso, E.M., Sugiarto, I., 2019. Spectral Analysis of Familiar Human Voice Based On Hilbert-Huang Transform,
- 569 in: 2018 International Conference on Computer Engineering, Network and Intelligent Multimedia, CENIM 2018 - Proceeding. doi:10.1109/CENIM.2018.8710943.
- 570 Huang, N.E., 2014. Hilbert-Huang transform and its applications. volume 16. World Scientific.
- 571 Huang, N.E., Attoh-Okine, N.O., 2005. The Hilbert-Huang transform in engineering. CRC Press.
- 572 Huang, N.E., Shen, Z., Long, S.R., Wu, M.C., Snin, H.H., Zheng, Q., Yen, N.C., Tung, C.C., Liu, H.H., 1998. The empirical mode decomposition
- 573 and the Hubert spectrum for nonlinear and non-stationary time series analysis. Proceedings of the Royal Society A: Mathematical, Physical and
- 574 Engineering Sciences doi:10.1098/rspa.1998.0193.
- 575 Kawabata, Y., Takahashi, T., Haginoya, T., Shirakashi, M., 2013. Interference Effect of Downstream Strip-Plate on the Crossflow Vibration of a
- 576 Square Cylinder. Journal of Fluid Science and Technology 8, 647–658. doi:10.1299/jfst.8.348.
- 577 Khalak, A., Williamson, C., 1999. Motions, Forces And Mode Transitions In Vortex-Induced Vibrations At Low Mass-Damping. Journal of Fluids
- 578 and Structures 13, 813–851. URL: <http://www.sciencedirect.com/science/article/pii/S0889974699902360>, doi:10.1006/jfls.1999.0236.
- 579 Koide, M., Kato, N., Yamada, S., Kawabata, Y., Takahashi, T., Shirakashi, M., 2007. Influence Of A Cruciform Arrangement Downstream Strip-
- 580 Plate On Crossflow Vibration. Journal of Computational and Applied Mechanics 8, 135–148.
- 581 Koide, M., Ootani, K., Yamada, S., Takahashi, T., Shirakashi, M., 2006. Vortex Excitation Caused by Longitudinal Vortices Shedding from
- 582 Cruciform Cylinder System in Water Flow. JSME International Journal 49, 1043–1048.
- 583 Koide, M., Sekizaki, T., Yamada, S., Takahashi, T., Shirakashi, M., 2009. A Novel Technique for Hydroelectricity Utilizing Vortex Induced
- 584 Vibration, in: Proceedings of the ASME Pressure Vessels and Piping Division Conference, PVP2009-77487.
- 585 Koide, M., Sekizaki, T., Yamada, S., Takahashi, T., Shirakashi, M., 2013. Prospect of Micro Power Generation Utilizing VIV in Small
- 586 Stream Based on Verification Experiments of Power Generation in Water Tunnel. Journal of Fluid Science and Technology 8, 294–
- 587 308. URL: https://www.jstage.jst.go.jp/article/jfst/8/3/8{_}294/{}_articlehttp://jlc.jst.go.jp/DN/JST.JSTAGE/

Lift Evolution in a Pure Cruciform Energy Harvester

- 591 jfst/8.294?lang=en{&}from=CrossRef{&}type=abstract, doi:10.1299/jfst.8.294.
- 592 Koide, M., Takahashi, T., Shirakashi, M., Salim, S.A.Z.B.S., 2017. Three-dimensional structure of longitudinal vortices shedding from cruciform
593 two-cylinder systems with different geometries. *Journal of Visualization*, 1–11.
- 594 Langley Research Centre, 2018. Turbulence Modeling Resource. URL: <https://turbmodels.larc.nasa.gov/>.
- 595 Maruai, N.M., Ali, M.S.M., Ismail, M.H., Zaki, S.A., 2018. Flow-induced vibration of a square cylinder and downstream
596 flat plate associated with micro-scale energy harvester. *Journal of Wind Engineering and Industrial Aerodynamics* 175, 264–
597 282. URL: [https://www.scopus.com/inward/record.uri?eid=2-s2.0-85042219159&doi=10.1016%2Fj.jweia.2018.01.010](https://www.scopus.com/inward/record.uri?eid=2-s2.0-85042219159&doi=10.1016%2Fj.jweia.2018.01.010&partnerID=40&md5=2f3f62b94bb69ced3368b32e682aefc7).
- 598 Maruai, N.M., Mat Ali, M.S., Ismail, M.H., Shaikh Salim, S.A.Z., 2017. Downstream flat plate as the flow-induced vibration enhancer for energy har-
599 vesting. *Journal of Vibration and Control*, 107754631770787 URL: <http://journals.sagepub.com/doi/10.1177/1077546317707877>,
600 doi:10.1177/1077546317707877.
- 601 Mat Ali, M.S., Doolan, C.J., Wheatley, V., 2011. Low Reynolds number flow over a square cylinder with a splitter plate. *Physics of Fluids* 23,
602 doi:10.1063/1.3563619.
- 603 Nguyen, T., Koide, M., Yamada, S., Takahashi, T., Shirakashi, M., 2012. Influence of mass and damping ratios on VIVs of a cylinder with a
604 downstream counterpart in cruciform arrangement. *Journal of Fluids and Structures* 28, 40–55. doi:10.1016/j.jfluidstructs.2011.10.
605 006.
- 606 Raghavan, K., 2007. Energy Extraction from a Steady Flow Using Vortex Induced Vibration. Doctoral dissertation. The University of Michigan.
607 URL: <http://deepblue.lib.umich.edu/handle/2027.42/55687>.
- 608 Raghavan, U., Albert, R., Kumara, S., 2007. Near linear time algorithm to detect community structures in large-scale networks. *Phys. Rev E* 76,
609 036106.
- 610 Richardson, L.F., Gaunt, J.A., 1927. The deferred approach to the limit. *Philosophical Transactions of the Royal Society A* doi:<https://doi.org/10.1098/rsta.1927.0008>.
- 611 Shirakashi, M., Mizuguchi, K., Bae, H.M., 1989. Flow-induced excitation of an elastically-supported cylinder caused by another located downstream
612 in cruciform arrangement. *Journal of Fluids and Structures* 3, 595–607. doi:10.1016/S0889-9746(89)90150-3.
- 613 Stern, F., Wilson, R.V., Coleman, H.W., Paterson, E.G., 2001. Comprehensive approach to verification and validation of CFD simulations^{if};part 1:
614 methodology and procedures. *Journal of fluids engineering* 123, 793–802.
- 615 Sun, H., Kim, E.S., Nowakowski, G., Mauer, E., Bernitsas, M.M., 2016. Effect of mass-ratio, damping, and stiffness on optimal hydrokinetic energy
616 conversion of a single, rough cylinder in flow induced motions. *Renewable Energy* 99, 936–959. URL: <http://www.sciencedirect.com/science/article/pii/S0960148116306206>, doi:10.1016/j.renene.2016.07.024.
- 617 Wu, W., 2011. Two-Dimensional RANS Simulation of Flow Induced Motion of Circular Cylinder with Passive Turbulence Control. Doctoral
618 dissertation. The University of Michigan.
- 619 Wu, Z., Huang, N.E., 2008. Ensemble Empirical Mode Decomposition: A Noise-Assisted Data Analysis Method. *Advances in Adaptive Data
620 Analysis* doi:10.1142/s1793536909000047.
- 621 Zhang, B., Mao, Z., Song, B., Ding, W., Tian, W., 2018. Numerical investigation on effect of damping-ratio and mass-ratio on energy
622 harnessing of a square cylinder in FIM. *Energy* 144, 218–231. URL: <https://www.scopus.com/inward/record.uri?eid=2-s2.0-85037995662&doi=10.1016%2Fj.energy.2017.11.153&partnerID=40&md5=01db7c6b6d4d44e88de7045843c7d423>,
623 doi:10.1016/j.energy.2017.11.153.
- 624 Zhao, M., Lu, L., 2018. Numerical simulation of flow past two circular cylinders in cruciform arrangement. *Journal of Fluid Mechanics* 848, 1013–

Lift Evolution in a Pure Cruciform Energy Harvester

- 629 1039. URL: https://www.cambridge.org/core/product/identifier/S0022112018003804/type/journal_article, doi:10.
630 1017/jfm.2018.380.
- 631 Zhou, L., Meng, Y., Abbaspour, K.C., 2019. A new framework for multi-site stochastic rainfall generator based on empirical orthogonal function
632 analysis and Hilbert-Huang transform. *Journal of Hydrology* doi:10.1016/j.jhydrol.2019.05.047.